Chapter 2

Barotropic and Baroclinic Tidal Energy

Dujuan Kang

Additional information is available at the end of the chapter

http://dx.doi.org/10.5772/52293

1. Introduction

Oceans cover approximately 71% percent of the Earth's surface, which makes them the largest solar energy collector in the world. On the other hand, the seawater moves constantly at different scales ranging from large-scale ocean currents down to centimeter-scale turbulent motions. These movements create a huge store of kinetic energy in the ocean. The ocean energy is clean and renewable. Therefore, a better understanding of the physical processes that govern the ocean movements is crucial to utilize the ocean energy more efficiently.

The tides are one of the major sources of energy to mix the interior ocean. The barotropic tidal energy is converted into heat through a series of important mixing processes. When the barotropic tides flow over rough topographic features, a portion of the barotropic energy is lost directly through local mixing, while the other portion is converted into baroclinic energy through the generation of internal (baroclinic) tides. This generated baroclinic energy either dissipates locally or radiates into the open ocean, and then cascades into smaller scales along the internal wave spectrum and finally turns into deep ocean turbulence (Figure 1). In the past decade significant efforts have been made to understand these tidal mixing processes and the associated energy distributions. Munk & Wunsch (1998) proposed a global tidal energy flux budget as shown in Figure 1. Of the 3.5 TW (1 TW $= 10^{12}$ W) total tidal energy lost in the ocean, approximately 2.6 TW is dissipated in shallow marginal seas through bottom friction, while the remaining portion is lost in the deep ocean. Egbert & Ray (2000, 2001) have confirmed that approximately 1 TW, or 25–30% of the global total tidal energy is lost in the deep ocean by inferring dissipation from a global tidal model. They found the tides lose much more energy in the open ocean, generally in regions with rough topographic features (Figure 2). Field observations also showed that turbulent mixing is several order of magnitude larger over rough topography than over smooth abyssal plains [18]. This evidence has led to the interest in internal tides as a major source of energy for deep-ocean mixing. Both analytical and numerical investigations have also been performed to estimate the tidal energy flux budget [1, 9, 17, 20].

This chapter focuses on the numerical investigation of tidal energy in the ocean. The problem of how and where the ocean tides distribute their energy is discussed using a numerical study

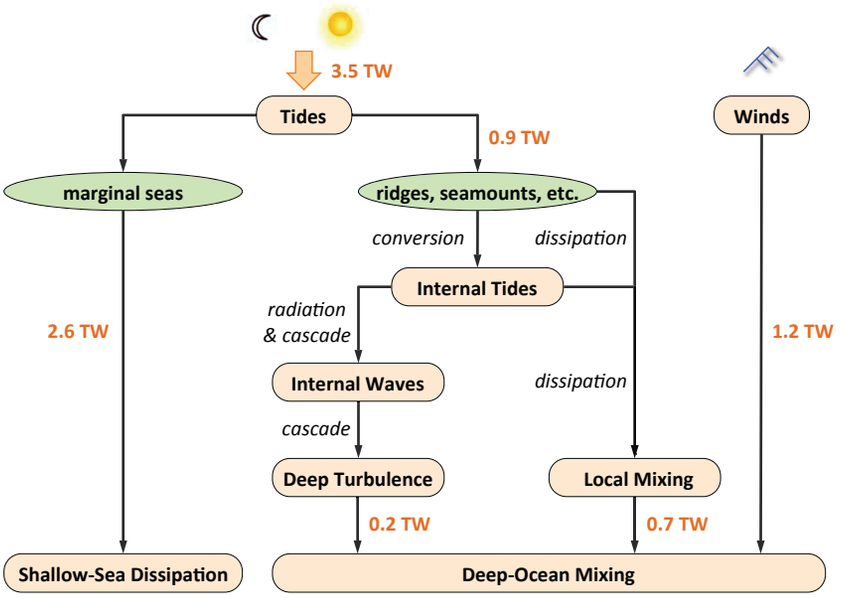

Figure 1. Global energy flux budget based on Munk and Wunsch (1998). The tides and winds are the two major sources of energy to mix the ocean. The tides contribute 3.5 TW of energy with 2.6 TW dissipated in shallow marginal seas and 0.9 TW lost in the deep ocean. The winds provide 1.2 TW of additional mixing power to maintain the global abyssal density distribution.

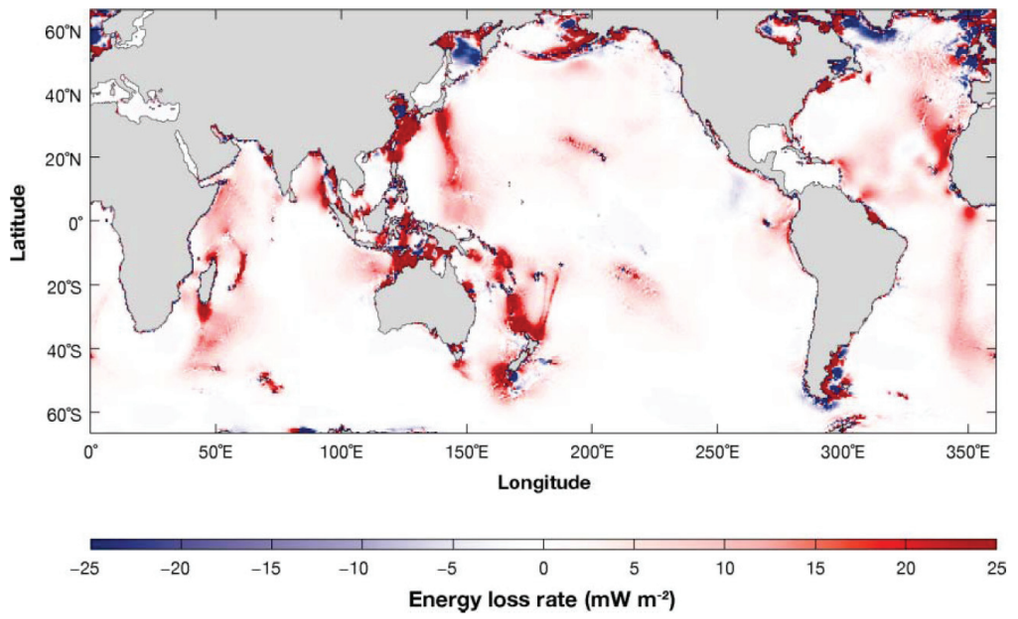

Figure 2. Global tidal energy loss rate derived from satellite altimetry sea-surface elevation data (Egbert and Ray, 2001).

of the tidal energetics in the Monterey Bay area along the central west coast of the United States. The purpose of this work is twofold: first, to provide a theoretical framework for the

accurate evaluation of tidal energy budget and, second, to conduct numerical simulations of barotropic and baroclinic tides for a given region in the ocean and estimate the tidal energy budget based on the theoretical framework. A brief derivation of the barotropic and baroclinic energy equations is presented in Section 2. Subsequent sections focus on the numerical simulations which include the model setup and tidal dynamics in Section 3, and the energetics analysis in Section 4. The characteristics of tidal energy conversion is examined in Section 5. Finally, conclusions are summarized in Section 6.

2. Theoretical framework

In order to study the energetics of barotropic and baroclinic tides, we derive the barotropic and baroclinic energy equations as a theoretical framework for the numerical evaluation of the tidal energy budget in subsequent sections. Here we provide a brief description of the equations. More detailed derivation can be found in Kang (2010).

The derivation is based on the three-dimensional Reynolds-averaged Navier-Stokes equations under the Boussinesq approximation, along with the density transport equation and the continuity equation,

$$\frac{\partial \mathbf{u}}{\partial t} + \mathbf{u}\cdot\nabla\mathbf{u} = -2\boldsymbol{\Omega}\times\mathbf{u} - \frac{1}{\rho_0}\nabla p - \frac{g}{\rho_0}\rho\mathbf{k} + \nabla_H\cdot(\nu_H\nabla_H\mathbf{u}) + \frac{\partial}{\partial z}\left(\nu_V\frac{\partial \mathbf{u}}{\partial z}\right), \tag{1}$$

$$\frac{\partial \rho}{\partial t} + \mathbf{u}\cdot\nabla\rho = \nabla_H\cdot(\kappa_H\nabla_H\rho) + \frac{\partial}{\partial z}\left(\kappa_V\frac{\partial \rho}{\partial z}\right), \tag{2}$$

$$\nabla\cdot\mathbf{u} = 0, \tag{3}$$

where $\mathbf{u} = (u, v, w)$ is the velocity vector and $\boldsymbol{\Omega}$ is the Earth's angular velocity vector. ν and κ, in units of $\mathrm{m}^2\ \mathrm{s}^{-1}$, are the eddy viscosity and eddy diffusivity, respectively. $(\ )_H$ and $(\ )_V$ are the horizontal and vertical components of a variable or operator. The total density is given by $\rho = \rho_0 + \rho_b + \rho'$, where ρ_0 is the constant reference density, ρ_b is the background density, and ρ' is the perturbation density due to wave motions. The pressure is split into its hydrostatic (p_h) and nonhydrostatic (q) parts with $p = p_h + q$, where the hydrostatic pressure can be further decomposed with $p_h = p_0 + p_b + p'$. To obtain the barotropic and baroclinic, the velocity is also split into its barotropic and baroclinic parts as $\mathbf{u} = \mathbf{U} + \mathbf{u}'$. Accordingly, the kinetic energy density, in units of $\mathrm{J\ m}^{-3}$, is decomposed as

$$E_k = \underbrace{\frac{1}{2}\rho_0\left(U^2 + V^2\right)}_{E_{k0}} + \underbrace{\frac{1}{2}\rho_0\left(u'^2 + v'^2 + w^2\right)}_{E'_k} + \underbrace{\rho_0\left(Uu' + Vv'\right)}_{E'_{k0}}, \tag{4}$$

where E_{k0} is the barotropic horizontal kinetic energy density, E'_k is the baroclinic kinetic energy density, and E'_{k0} is the cross term which vanishes upon depth-integration. Following Gill (1982), the perturbation potential energy due to surface elevation, in units of $\mathrm{J\ m}^{-2}$, is given by

$$\overline{E_{p0}} = \frac{1}{2}\rho_0 g\eta^2, \tag{5}$$

in which η is the free surface elevation. The available potential energy density, in units of $\mathrm{J\ m}^{-3}$, is defined as

$$E'_p = \int_{z-\zeta}^{z} g\left[\rho_b(z) + \rho'(z) - \rho_b(z')\right]dz', \tag{6}$$

where ζ is the vertical displacement of a fluid particle due to wave motions. This definition is an exact expression of the local APE because it computes the true active potential energy between the perturbed and unperturbed density profiles [12, 14].

Applying the variable decompositions and the boundary conditions, we obtain the depth-integrated barotropic and baroclinic energy equations as

$$\frac{\partial}{\partial t}\left(\overline{E_{k0}}+\overline{E_{p0}}\right)+\nabla_H\cdot\overline{\mathbf{F}_0}=-\overline{C}-\overline{\epsilon_0}-D_0\,, \tag{7}$$

$$\frac{\partial}{\partial t}\left(\overline{E'_k}+\overline{E'_p}\right)+\nabla_H\cdot\overline{\mathbf{F}'}=\overline{C}-\overline{\epsilon'}-D'\,, \tag{8}$$

where the depth-integrated barotropic and baroclinic energy flux terms, with the small unclosed terms neglected, are given by

$$\overline{\mathbf{F}_0}=\underbrace{\mathbf{U}_H\overline{E_{k0}}}_{\text{Advection}}\ \underbrace{+\mathbf{U}_H H\rho_0 g\eta+\mathbf{U}_H\overline{p'}+\mathbf{U}_H\overline{q}}_{\text{Pressure work}}\underbrace{-\overline{\nu_H\nabla_H E_{k0}}}_{\text{Diffusion}}, \tag{9}$$

$$\overline{\mathbf{F}'}=\underbrace{\overline{\mathbf{u}_H E'_k}+\overline{\mathbf{u}_H E_{k0}}+\overline{\mathbf{u}_H E'_p}}_{\text{Advection}}\underbrace{+\overline{\mathbf{u}'_H p'}+\overline{\mathbf{u}'_H q}}_{\text{Pressure work}}\underbrace{-\overline{\nu_H\nabla_H E'_k}-\overline{\kappa_H\nabla_H E'_p}}_{\text{Diffusion}}, \tag{10}$$

in which the contributions from energy advection, pressure work, and diffusion have been labeled. The definitions of the barotropic-to-baroclinic conversion rate ($\overline{C}$), the dissipation rates (ϵ_0 and ϵ') and the bottom drag terms (D_0 and D') are not listed here. Please refer to Kang (2010) for details.

The time-averaged forms of equations (7) and (8) are given by

$$\frac{1}{T}\Delta\overline{E_0}+\nabla_H\cdot\left\langle\overline{\mathbf{F}_0}\right\rangle=-\left\langle\overline{C}\right\rangle-\left\langle\overline{\epsilon_0}+D_0\right\rangle\,, \tag{11}$$

$$\frac{1}{T}\Delta\overline{E'}+\nabla_H\cdot\left\langle\overline{\mathbf{F}'}\right\rangle=\left\langle\overline{C}\right\rangle-\left\langle\overline{\epsilon'}+D'\right\rangle\,, \tag{12}$$

where $\langle\cdot\rangle=\frac{1}{T}\int_t^{t+T}(\cdot)\,d\tau$ is the time-average of a quantity over a time interval T. For a periodic system with period T, $\Delta\overline{E_0}$ and $\Delta\overline{E'}$ tend to zero and thus the first term in equations (11)-(12) vanishes. The remaining terms describe the energy balance associated with tidal dissipation processes. The $\nabla_H\cdot\left\langle\overline{\mathbf{F}_0}\right\rangle$ term represents the total barotropic energy that is available for conversion to baroclinic energy, $\left\langle\overline{C}\right\rangle$ represents the portion of the barotropic energy that is converted into baroclinic energy, and the $\nabla_H\cdot\left\langle\overline{\mathbf{F}'}\right\rangle$ term represents the portion of the converted baroclinic energy that radiates from the conversion site. Local dissipation occurs along with the conversion and radiation processes, and they are measured by the barotopic ($-\left\langle\overline{\epsilon_0}+D_0\right\rangle$) and baroclinic ($-\left\langle\overline{\epsilon'}+D'\right\rangle$) dissipation terms, respectively. This approach presents an exact measure of the barotropic-to-baroclinic tidal energy conversion.

3. Numerical simulations

We can implement the theoretical framework into a numerical ocean model and then use it to analyze the tidal energy budget. In this section, we provide an example of the numerical investigation of the tidal energetics in the Monterey Bay area along the central west coast of the United States.

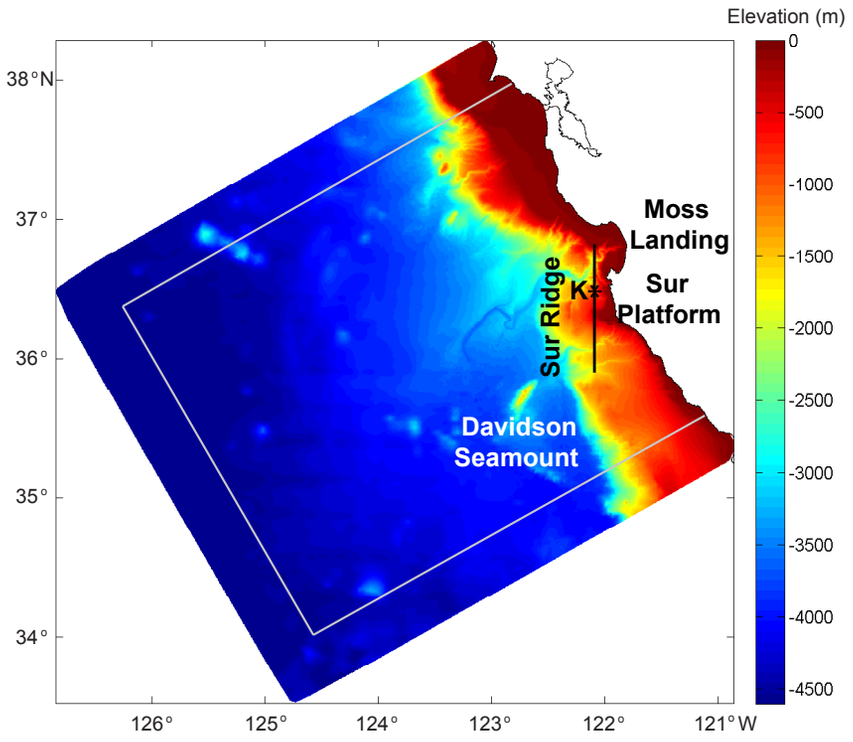

Figure 3. Bathymetry map of Monterey Bay and the surrounding open ocean. The black ∗ indicates a field observation station K. The domain outside the white box indicates the area affected by the sponge layers in the simulations. The solid black line indicates the vertical transaction along which baroclinic velocities are shown in Figure 5.

3.1. Model setup

Monterey Bay is featured by the prominent Monterey Submarine Canyon (MSC), numerous ridges, smaller canyons, and a continental slope and break region. This area is exposed to the large- and meso-scale variations of the California Current System as well as the tidal currents. Energetic internal wave activity has been observed in MSC and the surrounding region. Due to the complex bathymetry, tidal mixing processes in this area are of great interest. Our simulation domain extends approximately 200 km north and south of Moss Landing, and 400 km offshore (Figure 3), which is large enough to allow the evolution of offshore-propagating waves.

The ocean model we employ for this study is the SUNTANS model of Fringer *et al.* (2006). The resolution of the horizontal unstructured grid smoothly transitions from roughly 80 m within the Bay to 11 km along the offshore boundary. In the vertical, there are 120 z-levels with thickness stretching from roughly 6.6 m at the surface to 124 m in the deepest location, which provides better vertical resolution in the shallow regions. In total, the mesh consists of approximately 6 million grid cells in 3D.

The initial free-surface and velocity field are initialized as quiescent throughout the domain. The initial stratification is specified with horizontally-homogeneous temperature and salinity profiles. At the coastline, we apply the no-flow condition, while at the three open boundaries the barotropic velocities are specified with the OTIS global tidal model [2]. A sponge layer is imposed at each of the open boundaries to absorb the internal waves and minimize the

reflection of baroclinic energy into the domain. More model setup details and the validation of the model skill can be found in Kang and Fringer (2012).

3.2. Tidal dynamics

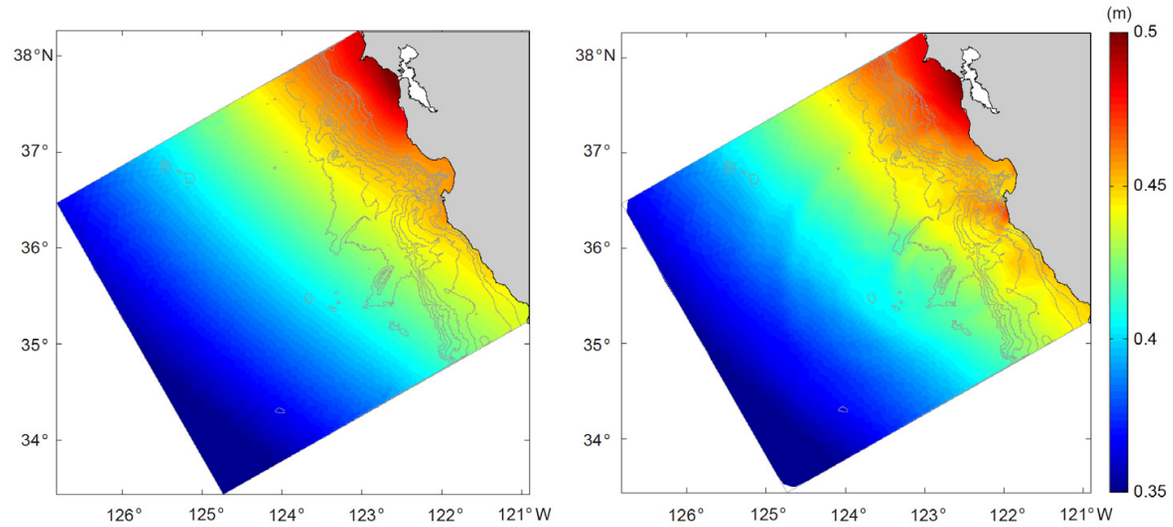

Figure 4. Sea surface elevation at $t = 18T_{M_2}$ from M_2 forced barotropic run (left) and baroclinic run (right). Bathymetry contours are spaced at -200, -500, -1000, -1500, -2000, -2500, -3000, -3500 m.

Monterey Bay is exposed to predominantly semidiurnal M_2 tide. Therefore we carry out two sets of M_2 forced simulations, one with homogeneous density to investigate the barotropic tides only, while the other with vertical stratification to study the baroclinic tides. Each simulation is run for 18 M_2 tidal cycles. Sea-surface elevations from such two runs are illustrated in Figure 4. This comparison highlights the modulation of baroclinic tides to the barotropic flow field, particularly near rough bottom topography.

Figure 5 demonstrates the vertical distribution of baroclinic velocities along a transect indicated in Figure 3. It can be seen clearly that baroclinic tides are generated at Sur Platform and then radiate to the north and south in the form of tidal beams.

4. Tidal energetics

We evaluate the depth-integrated, time-averaged barotropic and baroclinic energy equations (11) and (12) for the energy analysis in this section. They are averaged over the last six M_2 tidal cycles of the 18-M_2-cycle baroclinic simulation. Because the system is periodic, the first term in equation (11)-(12) tends to zero upon period-averaging. We therefore obtain the balance relations

$$\nabla_H \cdot \left\langle \overline{\mathbf{F}_0} \right\rangle = -\left\langle \overline{C} \right\rangle - \left\langle \overline{\epsilon_0} + D_0 \right\rangle , \tag{13}$$

$$\nabla_H \cdot \left\langle \overline{\mathbf{F}'} \right\rangle = \left\langle \overline{C} \right\rangle - \left\langle \overline{\epsilon'} + D' \right\rangle . \tag{14}$$

The model computes all the energy terms in the barotropic and baroclinic equations. In the following analysis, the conversion rate, $\left\langle \overline{C} \right\rangle$, and the energy flux divergence terms, $\nabla_H \cdot \left\langle \overline{\mathbf{F}_0} \right\rangle$

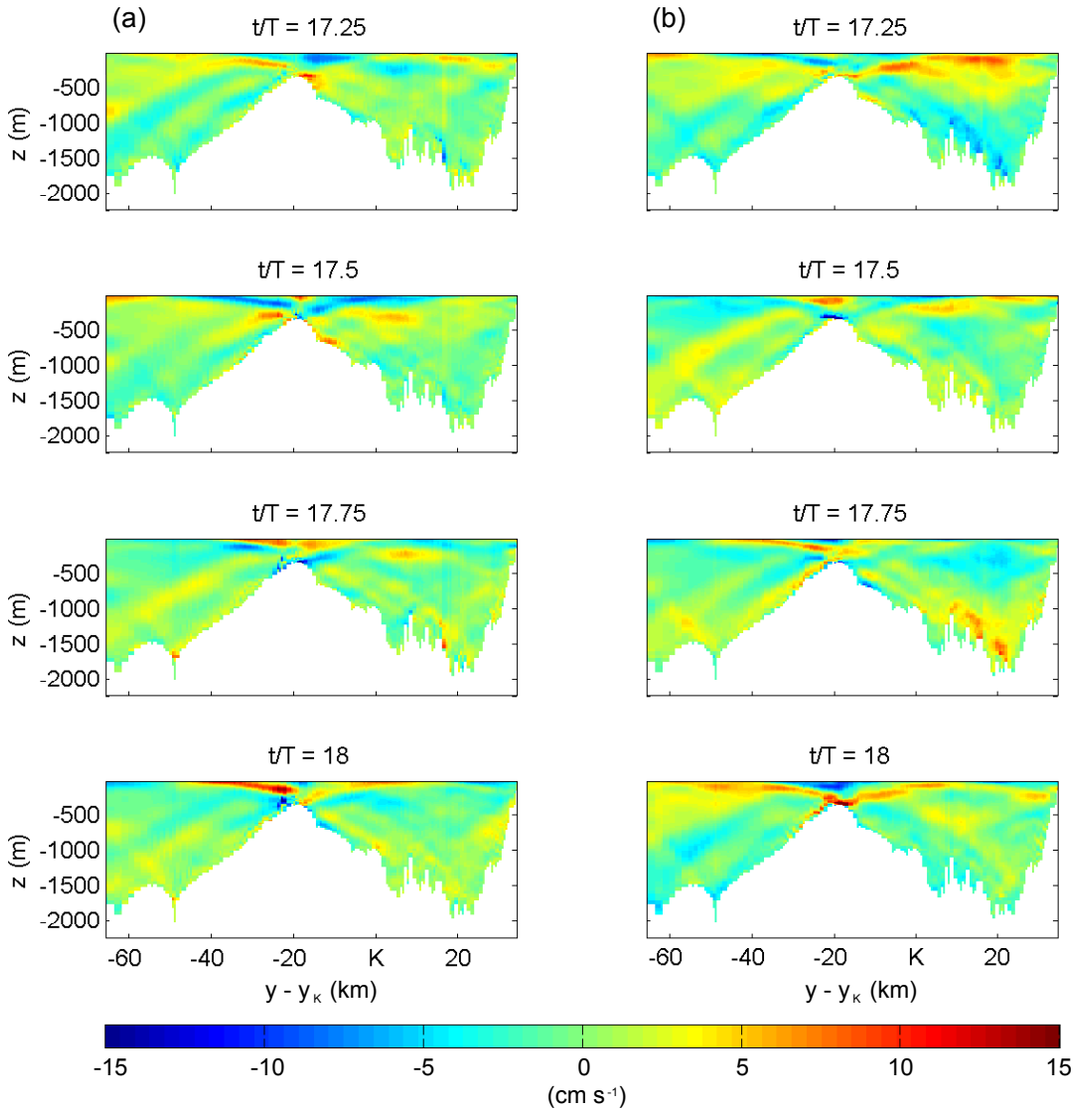

Figure 5. Vertical structure of the East-West (a) and North-South (b) baroclinic velocities along the transect indicated in Figure 3.

and $\nabla_H \cdot \langle \overline{\mathbf{F}'} \rangle$, are from direct model outputs. However, the barotropic and baroclinic dissipation rates are inferred from the above balance relations as in Niwa and Hibiya (2004).

4.1. Horizontal structure

The left panel of Figure 6 illustrates the horizontal distribution of the depth-integrated baroclinic energy flux vectors, $\langle \overline{\mathbf{F}'} \rangle$. Large energy fluxes are seen in the vicinity of rough topographical features, such as the MSC, the Sur Ridge-Platform region, and the Davidson Seamount. The right panel of Figure 6 shows the horizontal distribution of the depth-integrated barotropic-to-baroclinic conversion rate, $\langle \overline{C} \rangle$. Red color represents positive energy conversion rate, which implies generation of internal tides, and negative energy conversion rate (blue color) represents energy transfer from the baroclinic tide to the barotropic tide. Negative energy conversion is due to the phase difference between locally-

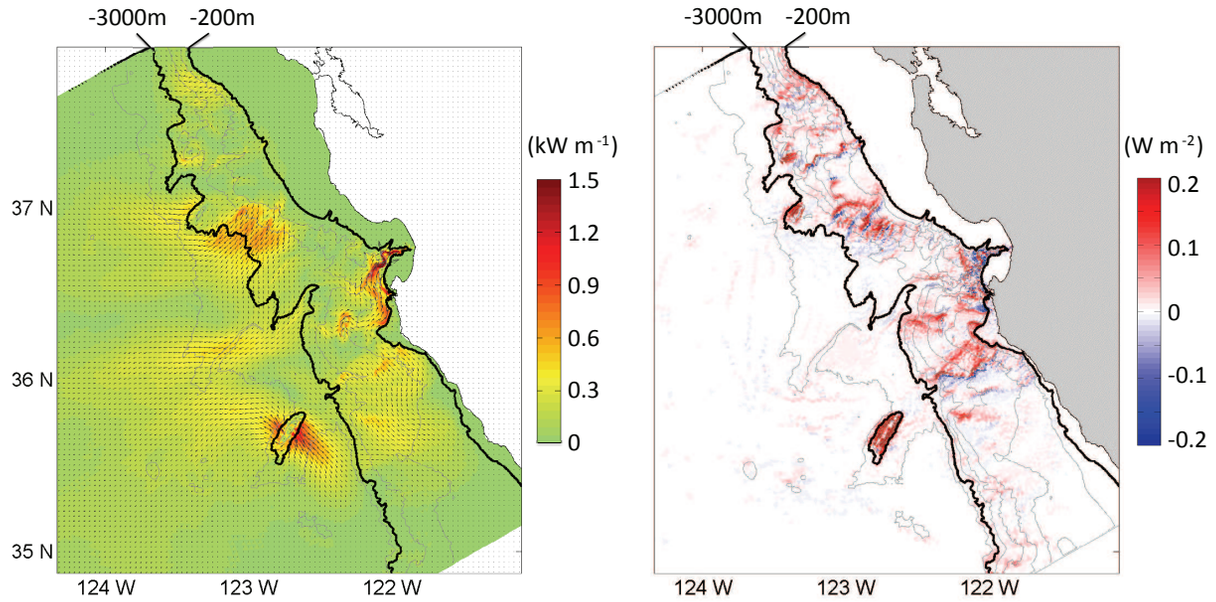

Figure 6. Depth-integrated, period-averaged baroclinic energy flux, $\left\langle \overline{\mathbf{F}'} \right\rangle$ (left), and barotropic-to-baroclinic conversion rate, $\langle \overline{C} \rangle$ (right). Darker bathymetry contours are 200 m and 3000 m isobaths.

and remotely-generated baroclinic tides, and therefore indicates multiple generation sites [23]. Significant negative conversion occurs within the MSC because the locally generated baroclinic tides interact with those generated at the North Sur Platform region. Large baroclinic energy can be seen radiating from North Sur Platform into the MSC following the canyon bathymetry from the figure. Figure 6 also shows that most of the generation is contained within the 200-m and 3000-m isobaths. The baroclinic energy flux divergence, $\nabla_H \cdot \left\langle \overline{\mathbf{F}'} \right\rangle$, and the baroclinic dissipation rate, $\nabla_H \cdot \left\langle \overline{\mathbf{F}'} \right\rangle - \langle \overline{C} \rangle$, are shown in Figure 7's left and right panels, respectively. Large baroclinic energy dissipation occurs near the locations of strong internal tide generation.

4.2. Energy flux budget

The total power within a region is obtained by area-integrating the period-averaged and depth-integrated energy terms to give

$$\text{BT Input} = -\sum \nabla_H \cdot \langle \overline{\mathbf{F}_0} \rangle \, \Delta A \,, \tag{15}$$

$$\text{Conversion} = \sum \langle \overline{C} \rangle \, \Delta A \,, \tag{16}$$

$$\text{BC Radiation} = \sum \nabla_H \cdot \left\langle \overline{\mathbf{F}'} \right\rangle \Delta A \,, \tag{17}$$

$$\text{BT Dissipation} = \sum \left(\nabla_H \cdot \langle \overline{\mathbf{F}_0} \rangle + \langle \overline{C} \rangle \right) \Delta A \,, \tag{18}$$

$$\text{BC Dissipation} = \sum \left(\nabla_H \cdot \left\langle \overline{\mathbf{F}'} \right\rangle - \langle \overline{C} \rangle \right) \Delta A \,, \tag{19}$$

where $\sum$ implies summation of the grid cells within a particular region and ΔA is the area of each grid cell.

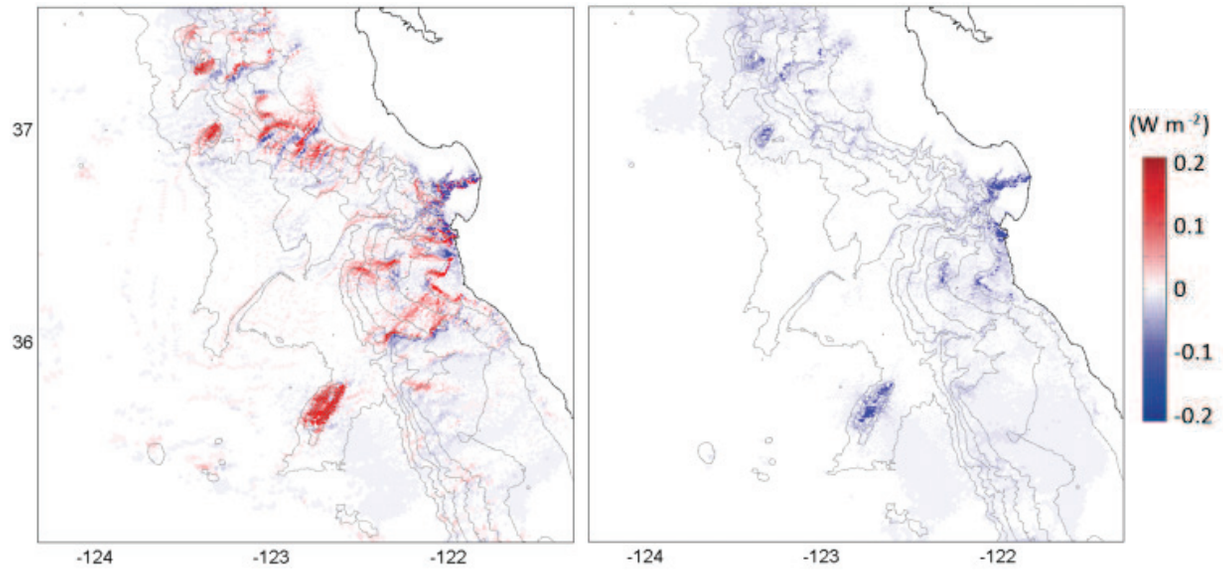

Figure 7. Depth-integrated, period-averaged baroclinic energy flux divergence, $\nabla_H \cdot \left\langle \overline{\mathbf{F}'} \right\rangle$ (left), and baroclinic dissipation rate, $\nabla_H \cdot \left\langle \overline{\mathbf{F}'} \right\rangle - \langle \overline{C} \rangle$ (right).

As Figure 6 indicated, most of the baroclinic energy generation is within the 200-m and 3000-m isobaths. We now depict the energy budget for the shelf and slope regions bounded by the 200-m and 3000-m isobaths Figure 8. Barotropic energy is lost at a rate of 147 MW to the slope region and approximately 87% of this energy is converted into baroclinic energy. Most of this generated baroclinic energy is dissipated locally, while the remaining portion (38%) is radiated. The shelf region acts as a baroclinic energy sink because it dissipates both the energy generated locally and the portion flowing into it from the slope region.

Two efficiency parameters are defined to examine the characteristics of baroclinic energy conversion and radiation, respectively,

$$\eta_c = \frac{\text{Conversion}}{\text{BT Input}}, \tag{20}$$

$$\eta_r = \frac{\text{BC Radiation}}{\text{Conversion}}. \tag{21}$$

Figure 9 compares the conversion and radiation efficiency for five subdomains (a)-(e). Subdomain (a), a 200 km $\times$ 230 km domain, is used to represent the Monterey Bay area because it includes all typical topographic features in this area. This comparison demonstrates that the tidal energy conversion and radiation depend strongly on topographic features. The Davidson Seamount and the Northern shelf-break region are the most efficient topographic features to convert ($\sim$ 94%) barotropic energy into baroclinic energy and then let it radiate out into the open ocean ($>$ 75%). The Sur Platform region also converts a large portion (88%) and radiates more than half of the barotropic energy as baroclinic energy. The MSC acts as an energy sink because it does not radiate energy but instead absorbs the baroclinic energy from the Sur Platform region.

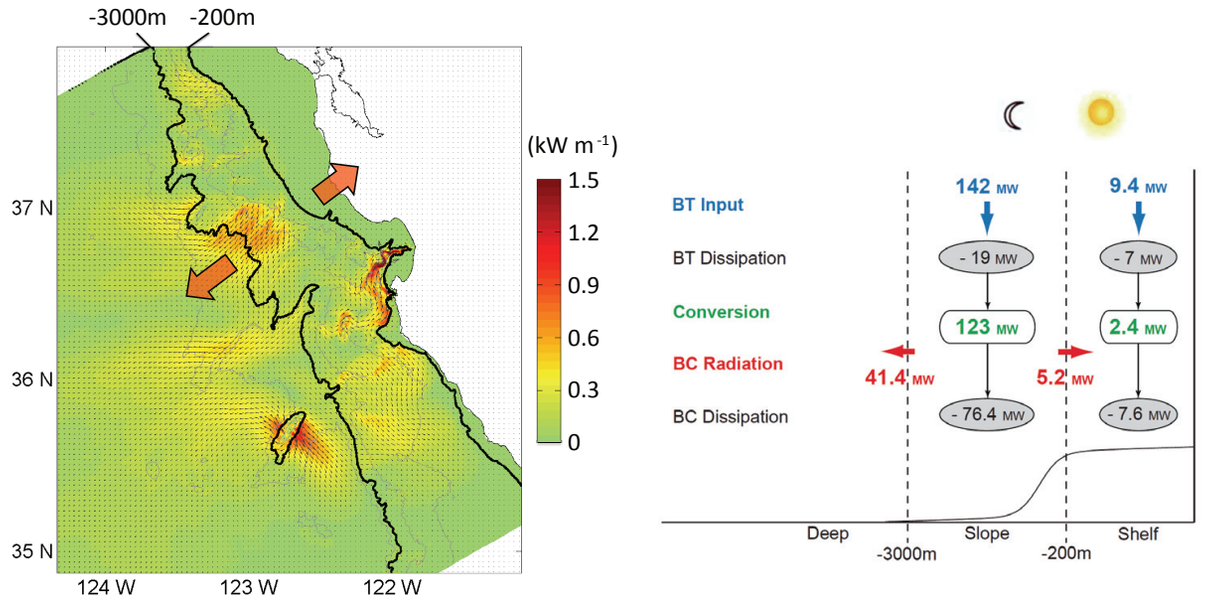

Figure 8. Schematic of the M_2 tidal energy budget for the two subdomains bounded by the 0-m, 200-m and 3000-m isobaths.

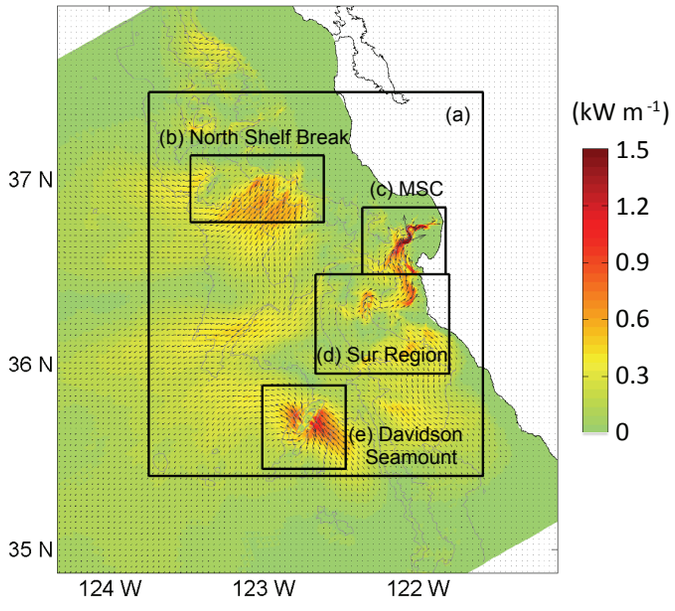

Region	η_c	η_r
(a) All	88%	42%
(b) Shelf Break	94%	76%
(c) Submarine Canyon	71%	-62%
(d) Ridge Platform	88%	61%
(e) Seamount	95%	81%

Figure 9. Efficiency of the M_2 baroclinic energy conversion and radiation for the five subdomains indicated in the left figure.

4.3. Energy flux contributions

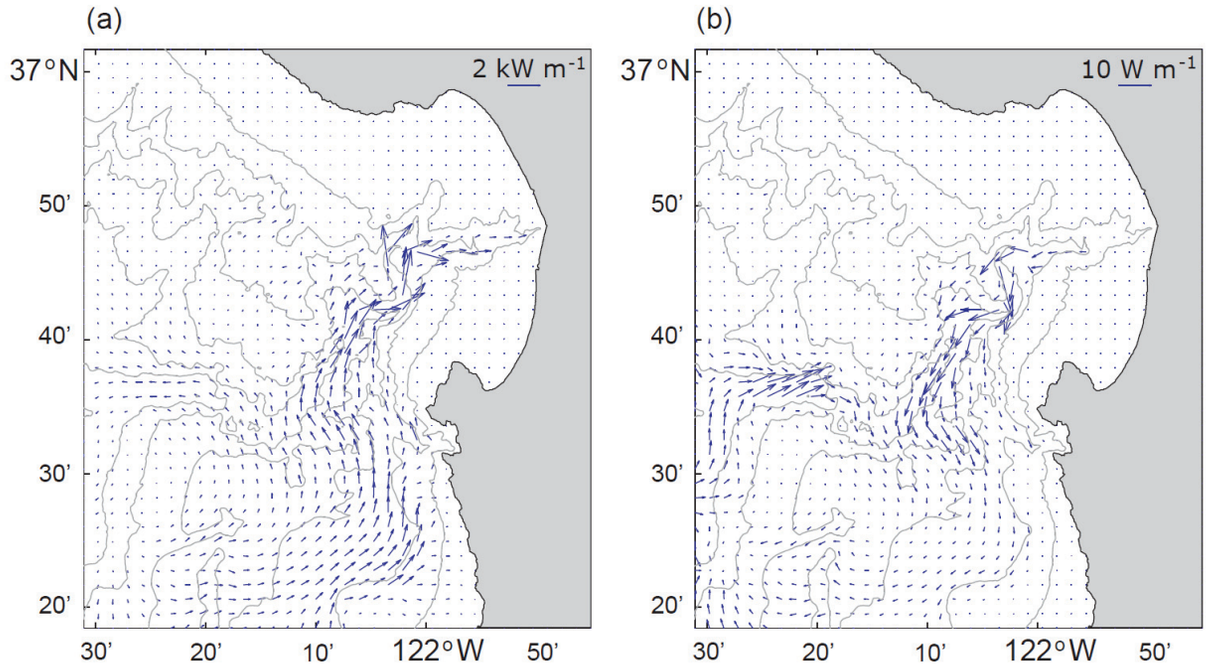

Figure 10. Baroclinic energy flux contributions from (a) hydrostatic, and (b) nonhydrostatic pressure work in the Monterey Submarine Cayon region.

As discussed in Section 2, our method computes the full energy fluxes and thus allows us to compare the contributions of different components. Here we choose subdomain (a) as our study domain. We found that the component due to hydrostatic pressure work (the traditional energy flux) is the dominant term. If we consider the total energy radiation as 100%, the hydrostatic contribution is $\sim 101\%$ while the other terms account for the remaining -1%. The advection and nonhydrostatic contributions are quite small, which implies that the internal tides in the Monterey Bay area are mainly linear and hydrostatic. Figure 10 shows that the hydrostatic and nonhydrostatic energy fluxes oppose one another within MSC. This occurs because the effect of the nonhydrostatic pressure is to restrict the acceleration owing to the impact of vertical inertia. Hydrostatic models therefore tend to overpredict the energy flux particularly for strongly nonhydrostatic flows.

5. Mechanism of energy conversion

Several nondimensional parameters are generally employed to discuss the character of barotropic-to-braoclinic energy conversion. The first parameter is the steepness parameter defined by

$$\epsilon_1 = \frac{\gamma}{s}, \tag{22}$$

where γ is the topographic slope, and s is the internal wave characteristic slope. The steepness parameter is used to distinguish between subcritical ($\epsilon_1 < 1$) and supercritical topography ($\epsilon_1 > 1$). The topography is referred to as critical when $\epsilon_1 = 1$.

The second nondimensional parameter is the tidal excursion parameter defined by

$$\epsilon_2 = \frac{U_0 k_b}{\omega}\,, \tag{23}$$

which measures the ratio of the tidal excursion U_0/ω to the horizontal scale of the topography k_b^{-1}.The excursion parameter is used to examine the nonlinearity of the waves [6, 15, 20]. When $\epsilon_2 \ll 1$, linear internal tides are generated mainly at the forcing frequency ω. Over subcritical topography ($\epsilon_1 < 1$) most of the energy generation is in the first mode internal tide, while over critical or supercritical topography ($\epsilon_1 \geq 1$), higher modes are generated and their superposition creates internal tidal beams. At intermediate excursion ($\epsilon_2 \sim 1$), nonlinearity becomes important, and nonlinear internal wave bores, weak unsteady lee waves, and solitary internal waves may be generated depending on the topographic features. When $\epsilon_2 > 1$, in addition to bores and solitary internal waves, strong unsteady lee waves may form [22].

Although internal wave generation is a complex process, we can summarize the behavior of the internal wave generation in Monterey Bay by plotting histograms of the conversion and divergence terms as functions of the criticality and excursion parameters. Here we compute the two parameters throughout subdomain (a). The upper and left panels of Figures 11 demonstrate the distribution of conversion as a function of the nondimensional parameters ϵ_1 and ϵ_2, respectively. The energy conversion (green bins) occurs predominantly in regions within which $\epsilon_1 < 5$ and $\epsilon_2 < 0.02$. Under these conditions, baroclinic tides generated in this region are mainly linear and in the form of internal tidal beams [6, 20, 22]. As expected, conversion of barotropic energy into baroclinic energy peaks for critical topography near $\epsilon_1 \sim 1$. More interesting, however, is that there is also a peak in conversion for a particular value of $\epsilon_2 \sim 0.005$.

The lower right panel of Figure 11 depicts the distribution of the energy conversion as a function of the two parameters. Energy conversion occurs mainly in regions where ϵ_1 and ϵ_2 satisfy a particular relation. When both parameters are small, this relation is linear. As the values of the two parameters increase, the departure is weakly quadratic.

6. Summary

The tides are one of the main power to mix the ocean, which is the largest energy collector from the Earth-Moon system. A better understanding of how and where the tides lost their energy is very important to the climate and energy study. In this chapter, we present a numerical method to investigate the tidal energy conversion and estimate the tidal energy budget.

A theoretical framework for analyzing tidal energetics is derived based on the complete form of the barotropic and baroclinic energy equations that provide an accurate and detailed energy analysis. Three-dimensional, high-resolution simulations of the tides and waves in the Monterey Bay area are conducted using the hydrodynamic coastal SUNTANS ocean model. Based on the theoretical approach, model results are analyzed to address the question of how the barotropic tidal energy is partitioned between local barotropic dissipation and local generation of baroclinic energy, and then how much of this generated baroclinic energy is lost locally versus how much is radiated away for open-ocean mixing. Subdomain (a), a 200 km $\times$ 230 km domain, is used to represent the Monterey Bay area because it includes

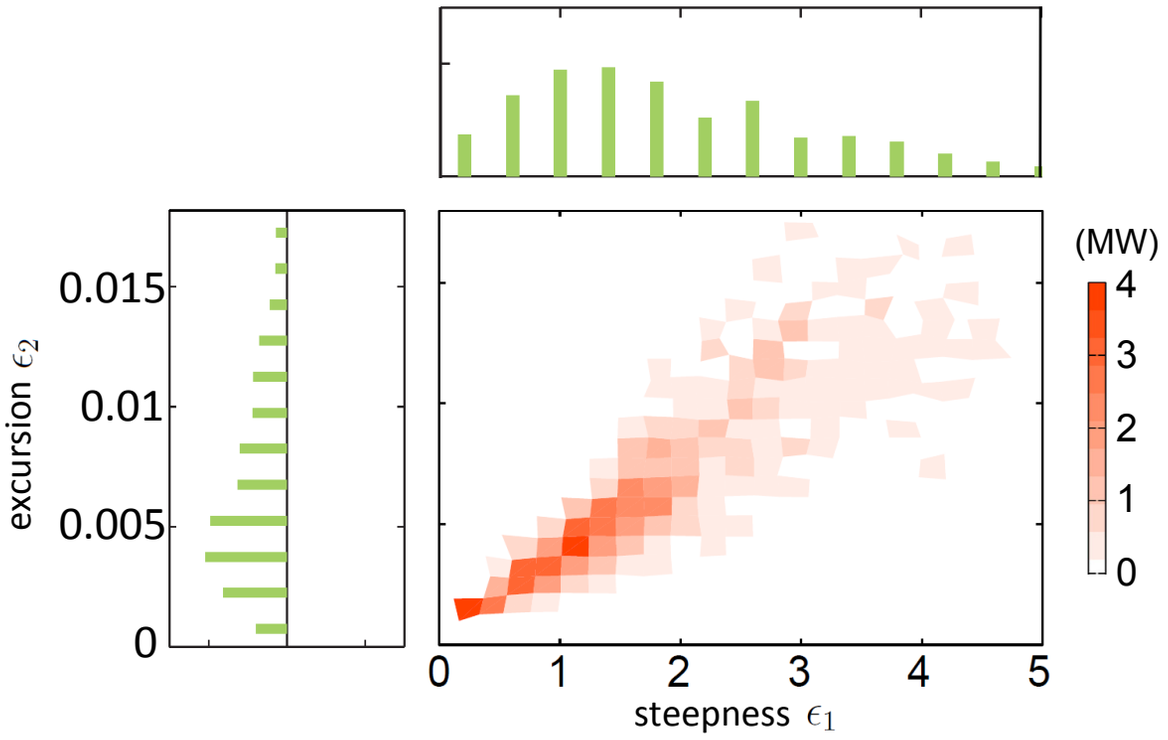

Figure 11. Distribution of the barotropic-to-baroclinic energy conversion as a function of steepness parameter ϵ_1 and excursion parameter ϵ_2 for subdomain (a).

all typical topographic features in this region. Of the 152 MW energy lost from the barotropic tide, approximately 133 MW (88%) is converted into baroclinic energy through internal tide generation, and 42% (56 MW) of this baroclinic energy radiates away for open-ocean mixing (Figure 12). The tidal energy partitioning depends greatly on the topographic features. The Davidson Seamount and the Northern shelf-break region are most efficient at baroclinic energy generation and radiation. The Sur Platform region converts a large portion and radiates roughly half of the barotropic energy as baroclinic energy. The Monterey Submarine Canyon acts as an energy sink because it does not radiate energy but instead absorbs the baroclinic energy from the Sur Platform region. The energy flux contributions from nonlinear and nonhydrostatic effects are also examined. The small advection and nonhydrostatic contributions imply that the internal tides in the Monterey Bay area are predominantly linear and hydrostatic.

We also investigate the character of tidal energy conversion by examining the energy distribution as a function of two nondimensional parameters, namely the steepness parameter ($\epsilon_1 = \gamma/s$) and the excursion parameter ($\epsilon_2 = U_0 k_b/\omega$). The generation mainly occurs in the regions satisfying $\epsilon_1 < 5$ and $\epsilon_2 < 0.02$, indicating that baroclinic tides generated in the Monterey Bay area are mainly linear and in the form of internal tidal beams. The results highlight how description of the conversion process with simple nondimensional parameters produces results that are consistent with theory, in that internal wave energy generation peaks at critical topography ($\epsilon_1 \sim 1$). The results also indicate that conversion peaks for a particular excursion parameter ($\epsilon_2 \sim 0.005$ for this case). This implies that it may be possible to parameterize conversion of barotropic to baroclinic energy in barotropic models

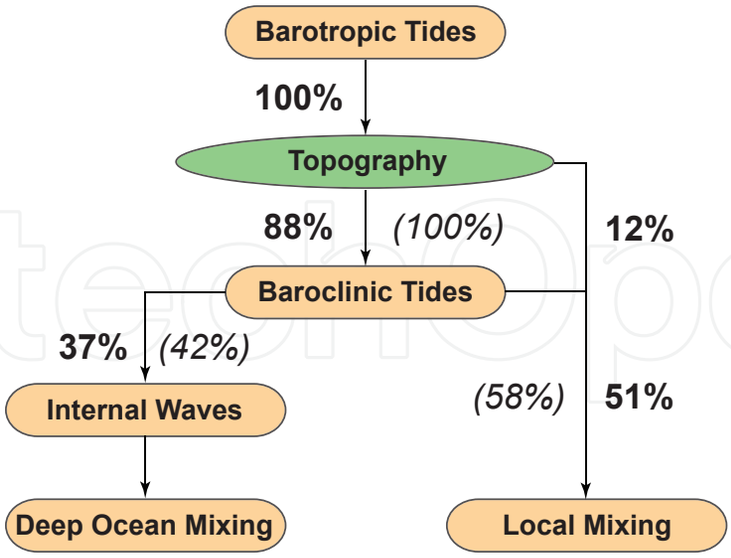

Figure 12. Schematic of the M_2 tidal energy budget in percentages for subdomain (a) indicated in Figure 9. The bold percentages are relative to the total input barotropic energy, and the thin italic percentages are relative to the generated baroclinic energy.

with knowledge of ϵ_1 and ϵ_2. For example, a parameterization of internal wave generation based on the steepness parameter has been widely used in global barotropic tidal models [21] and ocean general circulation models [10].

This work outlines a systematic approach to analyze internal tide energetics and estimate tidal energy budget regionally and globally. The results draw a picture of how the M_2 tidal energy is distributed in the Monterey Bay region. The Monterey Bay area is exposed to the large-scale California Current System and meso-scale eddies and upwelling. The seasonally varying dynamics may affect the stratification and thus the generation and propagation of internal tides in this area. Therefore, it may be necessary to consider seasonal effects of stratification and to include mesoscale effects by coupling with a larger-scale regional model such as ROMS [8, 19].

Acknowledgements

The author gratefully acknowledge the support of Professor Oliver Fringer at Stanford University and the ONR Grant. I would like to thank Samantha Terker, Drs. Jody Klymak, Robert Pinkel, James Girton, and Eric Kunze for kindly providing the field data. The helpful discussions with Drs. Robert Street, Stephen Monismith, Leif Thomas, and Rocky Geyer are greatly appreciated. I also thank Dr. Steven Jachec for useful help with simulation setup.

Author details

Dujuan Kang
Institute of Marine and Coastal Sciences, Rutgers University, New Jersey, USA

7. References

[1] Carter G.S (2010) Barotropic and baroclinic M2 tides in the Monterey Bay region. J. Phys. Oceanogr. 40: 1766-1783.

[2] Egbert G.D, Erofeeva S.Y (2002) Efficient inverse modeling of barotropic ocean tides. J. Atmos. Oceanic Technol. 19: 183-204.

[3] Egbert G.D, Ray R.D (2000) Significant dissipation of tidal energy in the deep ocean inferred from satellite altimeter data. Nature. 405: 775-778.

[4] Egbert G.D, Ray R.D (2001) Estimates of M2 tidal energy dissipation from TOPEX/Poseidon altimeter data. J. Geophys. Res. 106(C10): 22475-22502.

[5] Fringer O.B, Gerritsen M, Street R.L (2006) An unstructured-grid, finite-volume, nonhydrostatic, parallel coastal ocean simulator. Ocean Modelling. 14: 139-173.

[6] Garrett C, Kunze E (2007) Internal tide generation in the deep ocean. Annu. Rev. Fluid Mech. 39: 57-87.

[7] Gill A.E (1982) Atmosphere-Ocean Dynamics. Academic Press.

[8] Haidvogel D.B, Arango H.G, Hedstrom K, Beckmann A, Malanotte-Rizzoli P, Shchepetkin A.F, 2000: Model evaluation experiments in the North Atlantic Basin: Simulations in nonlinear terrain-following coordinates. Dyn. Atmos. Oceans. 32: 239-281.

[9] Jachec S.M, Fringer O.B, Gerritsen M.G, Street R.L (2006) Numerical simulation of internal tides and the resulting energetics within Monterey Bay and the surrounding area. Geophys. Res. Lett. 33: L12605, doi:10.1029/2006GL026314.

[10] Jayne S.R (2009) The impact of abyssal mixing parameterizations in an ocean general circulation model. J. Phys. Oceanogr. 39: 1756-1775.

[11] Kang D. (2010) Energetics and dynamics of internal tides in Monterey Bay using numerical simulations. Ph.D. Dissertation. Stanford University. 170 p.

[12] Kang D, Fringer O.B (2010) On the calculation of available potential energy in internal wave fields. J. Phys. Oceanogr. 40: 2539-2545.

[13] Kang D, Fringer O.B (2012) Energetics of barotropic and baroclinic tides in the Monterey Bay area. J. Phys. Oceanogr. 42: 272-290.

[14] Lamb K.G (2007) Energy and pseudoenergy flux in the internal wave field generated by tidal flow over topography. Cont. Shelf Res. 27: 1208-1232.

[15] Legg S, Huijts K.M.H (2006) Preliminary simulations of internal waves and mixing generated by finite amplitude tidal flow over isolated topography. Deep-Sea Res. II. 53: 140-156.

[16] Munk W, Wunsch C (1998) Abyssal recipes II: Energetics of tidal and wind mixing. Deep-Sea Res. 45: 1977-2010.

[17] Niwa Y, Hibiya T (2004) Three-dimensional numerical simulation of M2 internal tides in the East China Sea. J. Geophys. Res. 109: C04027, doi:10.1029/2003JC001923.

[18] Polzin K.L, Toole J.M, Ledwell J.R, Schmitt R.W (1997) Spatial variability of turbulent mixing in the abyssal ocean. Science. 276: 93-96.

[19] Shchepetkin A.F, McWilliams J.C (2005) The Regional Oceanic Modeling System: A split-explicit, free-surface, topography-following-coordinate ocean model. Ocean Modelling. 9: 347-404.

[20] St. Laurent L, Garrett C (2002) The role of internal tides in mixing the deep ocean. J. Phys. Oceanogr. 32: 2882-2899.

[21] St. Laurent L, Simmons H.L, Jayne S.R (2002) Estimating tidally driven mixing in the deep ocean. Geophys. Res. Lett. 29: 2106-2110.
[22] Vlasenko V, Stashchuk N, Hutter K (2005) Baroclinic Tides: Theoretical Modeling and Observational Evidence. Cambridge University Press.
[23] Zilberman N.V, Becker J.M, Merrifield M.A, Carter G.S (2009) Model estimates of M2 internal tide generation over Mid-Atlantic Ridge topography. J. Phys. Oceanogr. 39: 2635-2651.